Quasiclassical Trajectory Calculations of $Mg(3s3p^1P_1) + H_2$ ($v = 0$, $N = 1$) → MgH (v, N) + H: Trajectory and Angular Momentum Analysis on Improved ab Initio Potential Energy Surfaces

Yu-Ming Hung and King-Chuen Lin*

Department of Chemistry, National Taiwan University, Taipei, Taiwan 106, Republic of China, and Institute of Atomic and Molecular Sciences, Academia Sinica, P.O. Box 23-166, Taipei, Taiwan 106, Republic of China

Received: June 30, 2000; In Final Form: October 24, 2000

In the reaction of $Mg(3s3p^1P_1)$ with H_2, we have constructed a new version of ab initio potential energy surfaces (PESs) for $2A'$and $1A'$ states and their corresponding fit energy functions, on which 50 000 trajectory calculations are performed. The improvement of the current quasiclassical trajectory (QCT) calculations has made dynamical parameters more reliable than those reported previously. For instance, the obtained bimodal rotational distribution of MgH ($v = 0$), with a peak ratio of ca. 2:1 for the high-N to low-N components, is consistent with the experimental findings. The evaluated vibrational population ratio of ca. 0.52 for $v = 1$ to $v = 0$ is also within the range of observation, 0.7 ± 0.2. In addition, this work provides new information about the formation of MgH rotational levels via the angular momentum analysis. The trajectory calculations reveals the relation of the rotational distribution to the impact parameter, b, and the relative angle, ϵ, between the orbital and rotational angular momenta of the products. The MgH is preferentially populated in the high-N levels at small b but favors the low-N distribution at acute-angle ($<90°$) ϵ. The analysis of vector correlation provides insight into the behavior of the MgH rotational population.

I. Introduction

The reaction of $Mg(3s3p^1P_1)$ with H_2 has been studied for more than a decade.[1−10] Breckenridge and co-workers in the mid 1980s first found the rotational bimodality of MgH ($v = 0$ and 1) distributions, with the major components (∼90%) peaking at high quantum numbers, $N = 28-30$, and the minor components at approximately $N = 10$.[2,6] They reported a value of 0.7 ± 0.2 for the vibrational population ratio of $v = 1$ to $v = 0$. Since then, the related reaction mechanism has received a great deal of attention. From the experimental point of view, Breckenridge and co-workers[6] have observed an isotope effect on the MgH distribution, and Lin and Huang[7] have conducted the temperature dependence measurements. Their observations support the fact that two distinct microscopic pathways occurring in the exit channel contribute the rotational bimodality of the nascent MgH product.

In the studies of potential energy surface (PES) calculations, Blickensderfer et al. and Chaquin et al. have revealed that the current reaction should be dominated by an insertion mechanism.[1,5] For the collinear H-abstraction mechanism, a substantial energy barrier will be met.[5] On the basis of the impulsive model, the formation of the high-N component is attributed to the insertion mechanism. But for the low-N distribution, different interpretations have been proposed.

In a recent work, we have conducted detailed dynamical ab initio PES calculations at the level of complete active space self-consistent field (CASSCF) on the excited ($^1B_2$ or $^1A'$) and the ground ($^1A_1$ or $^1A'$) states.[9] The obtained PESs reveal that MgH is produced via a nonadiabatic transition. Two distinct reaction pathways are elicited by the collision complex MgH_2 around the surface crossing. In the first one, the bent intermediate, affected by a strong anisotropy of the ground-state potential, decomposes via a linear HMgH geometry. The resulting MgH is anticipated to populate in the high rotational and vibrational levels. In contrast, as a result of the intermediate decomposition along the Mg−H stretching coordinate, the second pathway produces MgH in the low rotational and vibrational levels. These two tracks may account for the MgH distributions reported previously and help to clarify the ambiguity that the impulsive model has left.[11]

The above comprehension of the reaction pathways is based on features of the coupling strength between the final states and the exit channel potential.[11,12] A quantitative analysis of the measured distributions still demands dynamical calculations. Therefore, in our previous work, a quasiclassical trajectory (QCT) calculation has been performed on the corresponding fit functions and resulted in the following outcomes.[10] First, the increase of collision energy leads to a decrease of reaction cross sections. Second, a bimodal feature is observed in the obtained rotational product distributions for both MgH $v = 0$ and MgH $v = 1$. Inspection of the individual trajectory reveals that the extent of anisotropic interaction in the exit-channel PES determines both the high-N and low-N MgH distributions. Third, the calculation of the angular product distribution indicates that the reaction proceeds predominantly via a linear collision complex. Finally, in agreement with the experimental findings, the vibrational product distribution decreases along with the quantum numbers. Nevertheless, the ratio of ∼0.3 for MgH ($v = 1$) to MgH ($v = 0$) is underestimated.

* Corresponding author. Fax: 886-2-23621483. E-mail: kclin@mail.ch.ntu.edu.tw.

10.1021/jp002352y CCC: $20.00
Published on Web 12/07/2000

The above QCT calculations have gained some insight into the dynamics parameters for the current reaction. However, several shortcomings are inherent in the previous version.[10] First, restricted to the scope of the ab initio PESs, the corresponding fit functions become less reliable once the interatomic separation is larger than 3.8 Å. Second, owing to the accuracy of the fit functions, we were impelled to terminate the trajectory calculations at a short interatomic separation and unable to foresee the end results. Third, 1200 trajectories in the previous calculation is too few for specific states. For this reason, this work is aimed to improve the QCT calculation on the basis of more complete ab initio PESs.

In this work, we have first constructed a new version of ab initio PESs at the CASSCF level for the excited and the ground states. The PESs scope has been extended to the asymptotic region, and the potential energy functions are fitted accordingly. Five thousand trajectories have been involved in the QCT calculation on the obtained energy functions. Different from aforementioned calculations,[10] this work has taken into account rotational effect of H_2. The resulting rotational distributions of MgH ($v = 0$ and 1) exhibit rotational bimodality with much better quality than those reported.[10] The inspection of individual trajectories shows that low-N and high-N trajectories evolve distinctly along the reaction coordinate. In addition, this work sheds light on the angular momentum analysis. Four types of vector correlation will be discussed to interpret the MgH rotational distributions.

II. PES Calculations and Three-body Fitting

Similar to the previous work,[9,10] we have employed the 6-31+G* basis set to calculate the ab initio potentials at the CASSCF level with a Gaussian 94 package. The calculation has involved four active electrons (two from the valence of Mg and two from H_2) and six active spaces (from 3s, 3p, and 4s of Mg and 1σ of H_2). To examine the reliability of the obtained potentials, we have calculated the asymptotic energy difference between the ground and the first excited states to be 4.7038 eV, which is only 105 cm^{-1} higher than the electronic transition of an isolated Mg, 4.6908 eV. The bond length and vibrational frequency of H_2 are also optimized to be 0.7301 Å and 4643 cm^{-1}, with errors of 1.52% and 5.5%, compared to the experimental findings 0.7414 Å and 4401 cm^{-1}, respectively.

The ab initio potentials are then fitted into the following three-body expansion function suggested by Sorbie and Murrell:[13,14]

$$V(r_1,r_2,r_3) = V^{(1)}_{Mg} + V^{(2)}_{MgH}(r_1) + V^{(2)}_{HH}(r_2) + V^{(2)}_{MgH}(r_3) + V^{(3)}(r_1,r_2,r_3) \quad (1)$$

The one-body term $V^{(1)}_{Mg}$ of 1A′ and 2A′ are 0 and 4.6908 eV, respectively. The MgH and HH two-body terms are described by an extended Rydberg function

$$V_i^{(2)} = -D_e(1 + a_1\rho_i + a_2\rho_i^2 + a_3\rho_i^3)\exp(-a_1\rho_i)$$
$$\rho_i = r_i - r_{i\,eq} \quad (2)$$

where D_e is the dissociation energy, $r_{i\,eq}$ is the equilibrium bond distance, and $i = 1$, 2, and 3 represents MgH, HH, and MgH, respectively. a_1, a_2, and a_3 are the Dunham expansion coefficients, which can be obtained by solving a set of coupled equations containing the first, second, third, and fourth derivatives of potentials at $\rho = 0$.[13,15] Finally, the three-body term can be expressed as the product of a polynomial, $P(r_i)$, and a range function, $T(r_i)$

$$V^{(3)}(r_1,r_2,r_3) = P(r_i)T(r_i) \quad (3)$$

$$P(r_i) = V^0(1 + \sum_i C_i\rho_i + \sum_{i\le j} C_{ij}\rho_i\rho_j + ...)$$
$$\rho_i = r_i - r_{i\,eq} \quad (4)$$

$$T(r_i) = (1 - \tanh \gamma_1 S_1/2)(1 - \tanh \gamma_2 S_2/2) \quad (5)$$

where

$$S_1 = \sqrt{1/2}(r_1 + r_3 - r_{1\,eq} - r_{3\,eq}) \quad (6)$$

$$S_2 = r_2 - r_{2\,eq} \quad (7)$$

In such an expression, $V^{(3)}$ becomes zero when any atom in the triatomic system is removed to infinity. Here P is a polynomial of up to the fourth order in the three internuclear distances and T is expressed in terms of symmetry coordinates. There are 26 parameters contained in the three-body term each for the excited and ground states. The optimization of these parameters, including V^0, r_1(MgH), r_2(HH), γ_1(MgH), γ_2(HH), and 21 coefficients in P, was achieved by least-squares fits to 221 ab initio points on the $2A'$ surface and 401 points on the $1A'$ surface. All parameters are listed in Table 1.

TABLE 1: Parameters of Potential Fittings

Two-Body Terms					
species	D_e/eV	r_{eq}/Å	a_1/Å^{-1}	a_1/Å^{-2}	a_1/Å^{-3}
MgH ($X^2\Sigma^-$)	1.3300	1.7297	4.0884	5.3667	3.2515
MgH ($A^2\Pi$)	1.6136	1.6788	3.8920	4.7550	2.7930
H_2	4.4742	0.7414	3.9610	4.0640	3.5740

Three-Body Terms		
parameter	excited state	ground state
V^0/eV	−0.8985	3.8930
r_{eq} (MgH)/Å	1.8853	2.0485
r_{eq} (HH)/Å	1.6863	1.2660
γ_1 (MgH)/Å^{-1}	0.4683	0.7679
γ_2 (HH)/Å^{-1}	0.6222	0.6253
C_1/Å	1.3585	−0.0236
C_2	3.3927	−0.0430
C_{11}/Å^{-2}	−1.7717	−0.2205
C_{22}	−1.5513	−0.5348
C_{12}	2.2802	0.0514
C_{13}	2.0154	0.6876
C_{111}/Å^{-3}	−0.4907	0.1385
C_{222}	−0.5248	0.2420
C_{112}	1.1446	−0.2693
C_{122}	0.8984	−0.1419
C_{133}	1.4571	−0.3771
C_{123}	−0.4346	−0.8033
C_{1111}/Å^{-4}	0.6393	0.1131
C_{2222}	0.3432	−0.0437
C_{1112}	−1.8422	−0.2308
C_{1122}	1.3682	0.2380
C_{1222}	−0.7840	0.0151
C_{1313}	−3.1730	0.0546
C_{1333}	4.7217	−0.1876
C_{1123}	2.4772	0.0565
C_{1223}	−0.2575	0.2244

Although the ab initio diabatic potential surfaces in C_{2v} symmetry are readily computed, the calculations of PESs near the crossing region in C_s geometry become difficult to converge, and less data thus obtained may be involved in the fitting. The subsequent fitted potential surfaces determine the crossing seam in the region of 1.5 Å ≤ r_1, r_2, r_3 ≤ 2.0 Å and $\theta = 40-60°$; θ is the bending angle of H−Mg−H. Figures 1and 2 show the fit energy function for the ground ($1A'$) and the excited state ($2A'$)

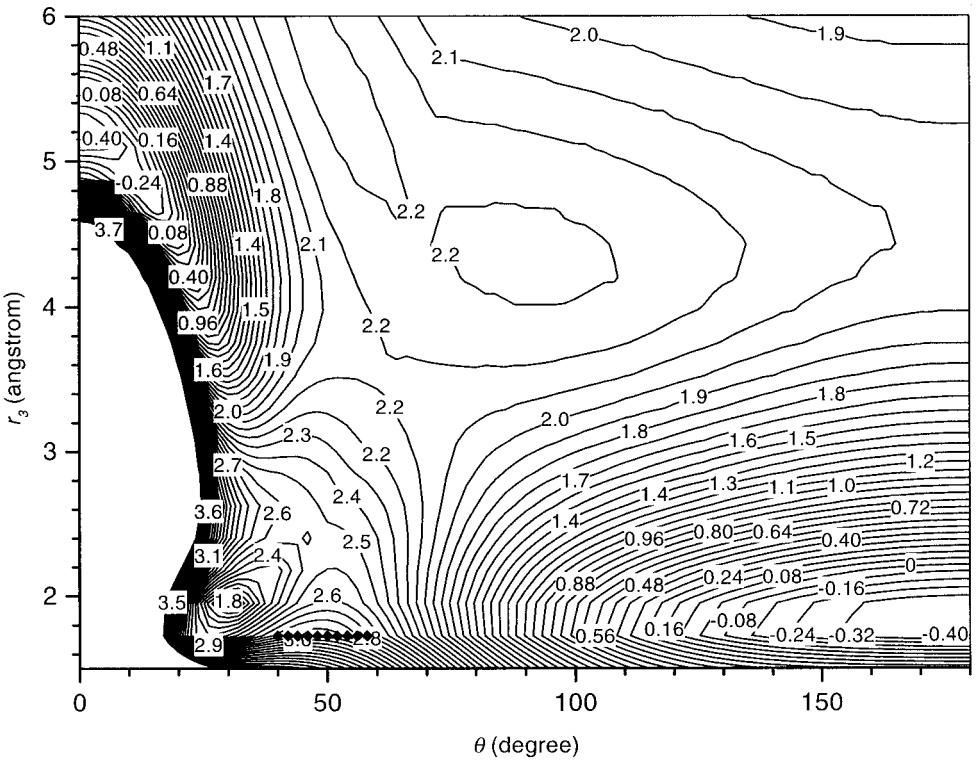

Figure 1. Contour plot of the 1A' surface as a function of MgH distance (r_3) and HMgH bending angle (θ), while the other MgH distance (r_1) is fixed at 1.74 Å, the equilibrium bond length of a free MgH. The reference potential energy as 0 eV corresponds to a C_{2v} configuration in which R, the distance between Mg and the center of H_2, is 6.0 Å and r_2 is 0.74 Å, the equilibrium distance of H_2. The symbol ◆ denotes the crossing seam.

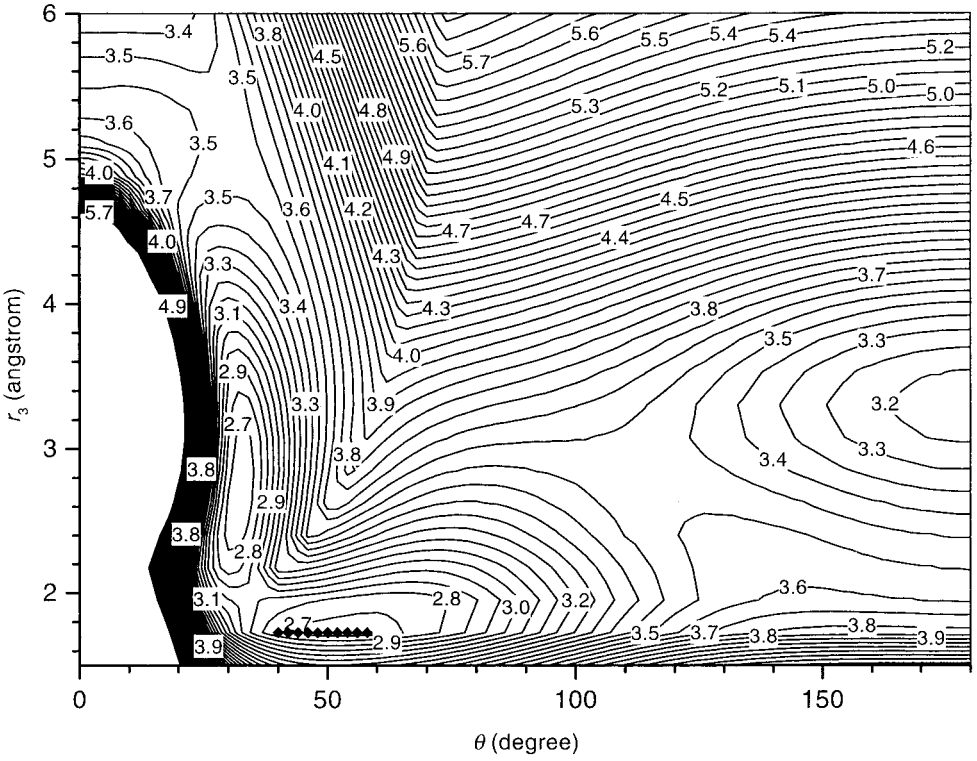

Figure 2. Contour plot of the 2A' surface as a function of MgH distance (r_3) and HMgH bending angle (θ), while the other MgH distance (r_1) is fixed at 1.74 Å, the equilibrium bond length of a free MgH. The reference potential energy as 0 eV corresponds to a C_{2v} configuration in which R, the distance between Mg and the center of H_2, is 6.0 Å and r_2 is 0.74 Å, the equilibrium distance of H_2. The symbol ◆ denotes the crossing seam.

surfaces. The equipotential contours are plotted as a function of the Mg−H (r_3) distance, 1.5 Å ≤ r_3 ≤ 6 Å, and the HMgH bending angle (θ), 0° ≤ θ ≤ 180°, while the other Mg−H (r_1) distance is fixed at 1.74 Å, the equilibrium distance of the product. The crossing seam between the 1A' and 2A' surfaces apparently occurs for the C_{2v} geometries. That is, the seam appears at $r_1 = r_3 = 1.74$ Å. The obtained χ^2 of fitting, which is indicative of the deviation from the ab initio energy, is 0.74 and 0.96 for 1A' and 2A', respectively.

In comparison with the old version, the PESs obtained in

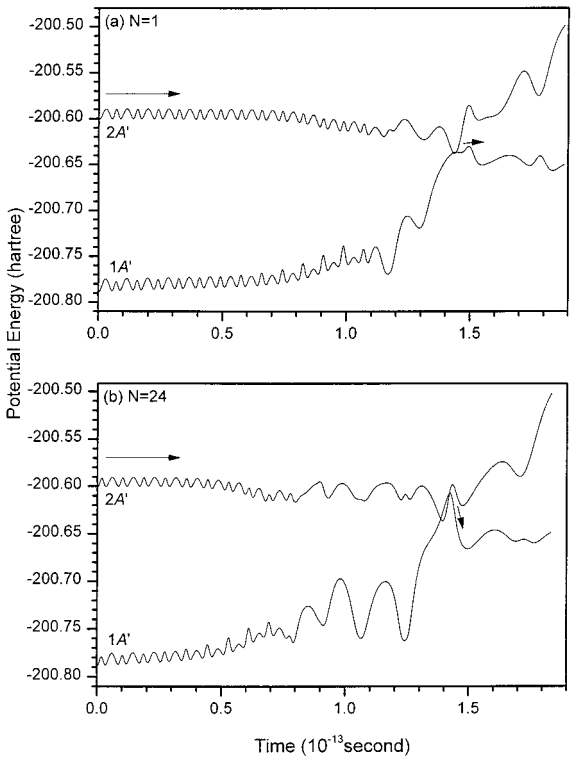

Figure 3. Potential curves $1A'$ and $2A'$ corresponding to the trajectories for MgH ($v = 0$, N): (a) $N = 1$ and (b) $N = 24$. Reactants are initially on $2A'$ and then change to $1A'$ at the contact point (a) or after the second crossing (b) between the two curves, as indicated by the arrows.

this work cover a much wider scope for varied geometric configurations. The old PES, although plotted similarly, lacks the information on the region of $\theta \leq 30°$ and $r_3 \geq 3$ Å. Two main features may be discerned from Figure 1. First, at $\theta > \sim 60°$ and $r_3 < \sim 3$ Å, the potential surface exhibits a strong angular dependence. The corresponding energy decreases dramatically with the angle expansion. The potential, as characterized by a strong coupling between radial and angular parts, tends to cause the product populated in the high rotational distribution. This feature has been found similarly in the previous work.[10] Second, the range of $\theta \leq 40°$ and $r_3 \geq 3$ Å, where the contour is characterized by a potential well, is beyond the scope of the old PES, which appears to have only a weak attractive potential within $30° \leq \theta \leq 40°$. This disparity results in a marked difference in the calculations of low-N trajectories.[10]

III. QCT Calculation

In the study, we adopt a Chapman's QCT program.[16,17] The initial collision energy (E_c) is 2.026 kcal/mol (~700 K). The temperature allows most H_2 molecules populated at $v = 0$ and $N = 1$ according to the Boltzmann law and keeps the initial H_2 energy in the quantum state of (v, N) = (0, 1) rather than that of (0, 0), as reported previously.[10] A random number generator is applied to sample the remaining initial conditions, including the impact parameter, the azimuthal and polar orientation angles of H_2 internuclear axis, the orientation of H_2 angular momentum, and the phase angle of H_2 vibration. To avoid repeated conditions to appear in the computation, we substitute the original linear congruential random number generator by a portable random number generator which has turned out to be successful.[18] The trajectories start on the $2A'$ potential surface at distance $R_o = 5.5$ Å between Mg and the center of the H_2 molecule and then evolve at a step of 0.2 fs to achieve energy conservation up to at least five figures. The maximum impact

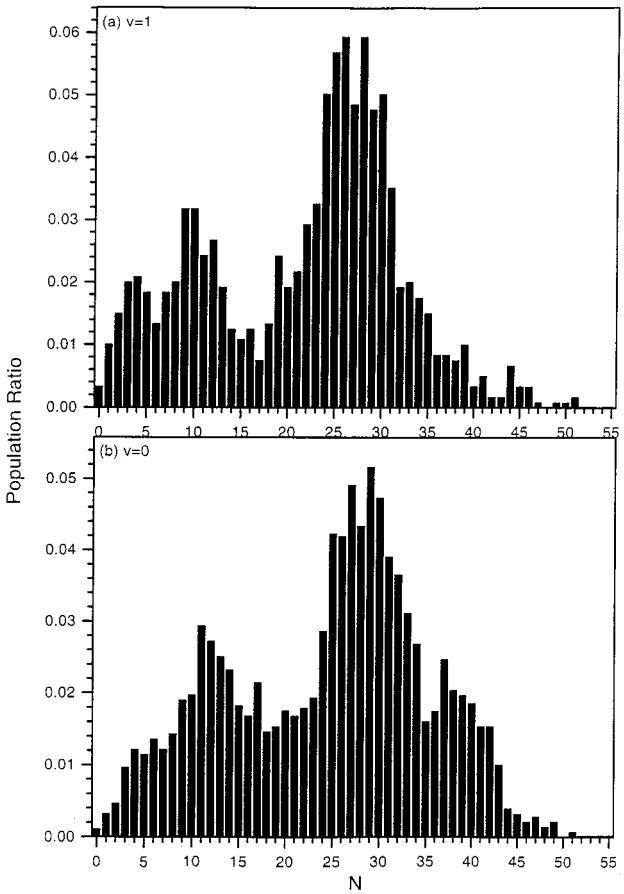

Figure 4. Rotational distributions of MgH in (a) $v = 1$ and (b) $v = 0$. H_2 is in the quantum level of $v = 0$ and $N = 1$. The initial kinetic energy is 2.026 kcal/mol.

parameter, $b_M = 4.8$ Å, is obtained by trajectory calculations with increasing b until the chemical reaction comes to nil. Here the MgH products are collected only within the range of r_1 (or r_3) ≤ 4.0 Å. Each trajectory is terminated in the exit channel at r_3 (or r_1) ≥ 6.0 Å, where the departing H is considered to be completely out of the influence of MgH.

The intersection between the adiabatic surfaces should be ideally a conical intersection. However, some fitting errors may cause the crossing seam to deviate from a conical intersection. For this case, the fit potential energies for the ground state within the crossing seam become higher than those for the excited state. For computational convenience, the transition probability is assumed to be unity when the trajectories go through the conical intersection and change to the lower surface (Figure 3a). However, if the crossing seam happens to be a nonconical intersection, the surface transition takes the following steps. First, the trajectories initially evolve on the excited-state surface prior to the surface crossing and after the first entry into the crossing seam. Then, as shown in Figure 3b, the trajectories switch instantaneously onto the ground-state surface at the second crossing, where the potential energy for the ground state is lower than that for the excited state. The cases for multiple crossings and recrossings are neglected. After trajectory computations are completed, the continuous distributions of the final vibrational and rotational energies contained in MgH are quantized into the state (v, N) with the aid of a harmonic oscillator and a rigid rotor model. If the obtained classical energies are within the halfway of the quantized energy gaps from a closest quantum state, then the portion of energy is assigned to this particular state.[19]

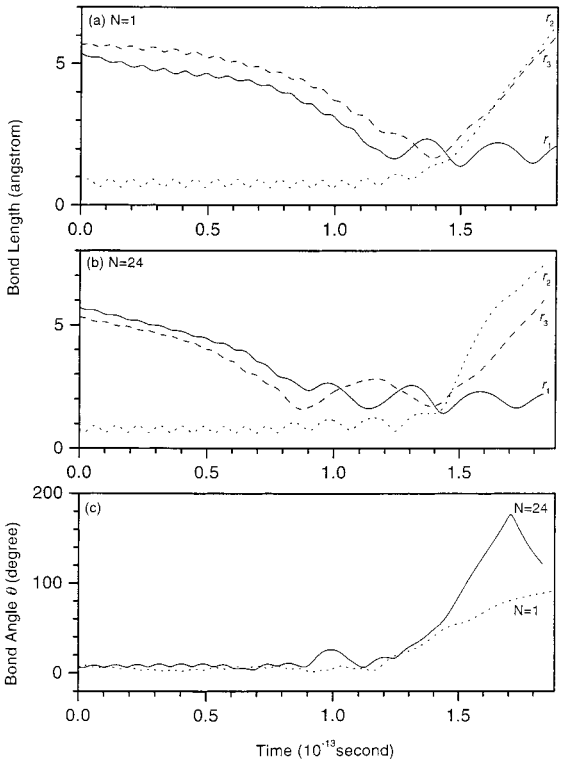

Figure 5. Evolution of trajectories for MgH ($v = 0$, N): (a) $N = 1$ and (b) $N = 24$. (c) Variation of the H−Mg−H angle. The corresponding interaction potentials are given in Figure 3.

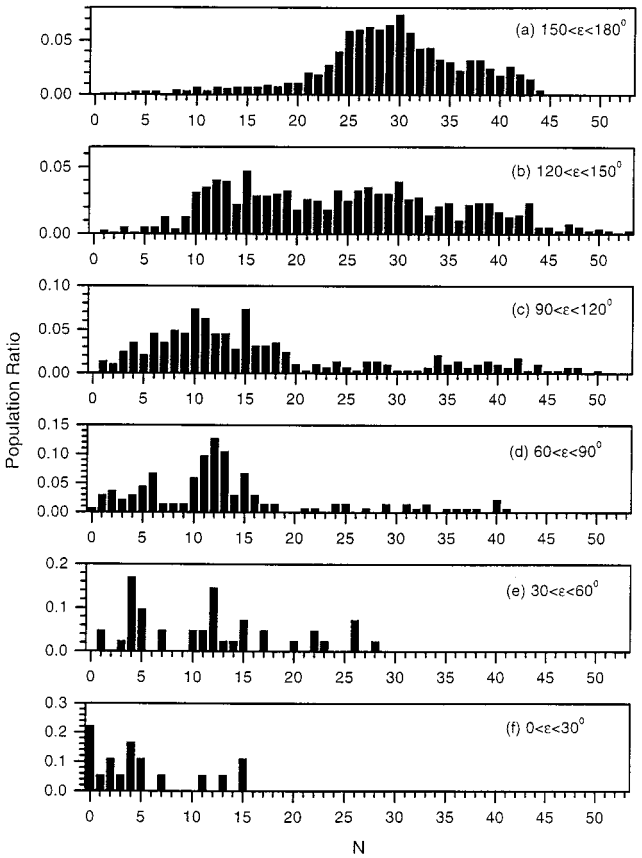

Figure 6. Rotational distribution of MgH ($v = 0$) vs ϵ, the relative angle between **l′** and **j′**. The initial kinetic energy is 2.026 kcal/mol, and H_2 is in $v = 0$ and $N = 1$. ϵ lies in the regions (a) (150°, 180°) with 1555 trajectories, (b) (120°, 150°) with 764 trajectories, (c) (90°, 120°) with 284 trajectories, (d) (60°, 90°) with 133 trajectories, (e) (30°, 60°) with 41 trajectories, and (f) (0°, 30°) with 18 trajectories.

IV. Results and Discussion

Improvement of QCT Calculation. In comparison with the previous work,[10] the current QCT calculations have made much improvement. First, the scopes of ab initio PESs for both $1A'$ and $2A'$ states have been extended to the asymptotic region (r_1, r_2, and $r_3 \geq 6.0$ Å), and the subsequent fit of the energy functions is based on these new PESs. The obtained fit parameters are more appropriate especially for application to the trajectory computation. Second, the trajectory starts at an initial interatomic separation of 5.5 Å, larger than the maximum impact parameter, b_M. This marks a sharp contrast to the previous QCT calculation. The latter, restricted to the fitting accuracy of the energy function, starts with the initial separation between Mg and H_2 at 3.4 Å and then terminates the trajectories at the Mg−H distance of ≤5 Å. Since the initial separation is smaller than b_M, the trajectory in the beginning has been exposed to the potential interaction. Thus, the trajectory performance may not sample over all the phase space and inevitably cause some uncertainty. In addition, the termination of the trajectory at brief time may hamper the completeness of the energy distribution in the final products and in turn affect the accuracy of the resulting vibrational and rotational distribution of MgH. Third, in this work, the increase of trajectories from1200 to 50 000 has effectively reduced the peak-to-peak deviation for the rotational distribution of MgH ($v = 0$) from ca. 0.014 to 0.0010.[20] We believe that the total number adopted is large enough to sample over all the phase space of the reaction channel. Furthermore, we have found that the randomly selected conditions repeat in about every 800 trajectories when adopting the original random number generator. Our substituting it with a portable random number generator results in no repeated calculations in 50 000 trajectories.[18] Fourth, the previous work fixed the initial energy of H_2 at (v, N) = (0, 0), ignoring the rotational effect on the chemical reaction. The adopted condition of H_2 at (0,1) in this work becomes consistent with that has been observed.[2,8]

The improvement of the current QCT calculations has resulted in more reliable dynamical parameters. For instance, Figure 4 shows the rotational distributions of MgH in the $v = 0$ and 1 levels. The rotational populations are characteristic of a bimodal distribution. The minor low-N component of MgH ($v = 0$) peaks at $N = 11$, while the major high-N component peaks at $N = 29$. A ratio of their peak heights corresponds to ~1:2, which is much closer to the experimental findings[2,6−8] than the previous ratio, 3:20.[10] The marked increase of the low-N population here is attributed to the attractive potential feature of the MgH_2 collision complex displayed in the range of $\theta \leq 40°$ and $r_3 \geq 3$ Å (Figure 1). The potential is characterized by a weak coupling between the radial and angular parts on the $1A'$ surface. This weak anisotropy enhances the number of low-N trajectories. When the individual rotational intensity of MgH are summed up to $N = 30$ (Figure 4a,b), the corresponding vibrational populations for the $v = 1$ and 0 levels yield a ratio of 0.52, which is within the range of the observation, 0.7 ± 0.2.[2] At $N > 30$, the experimental rotational spectra become congested and inseparable.[2,6−8]

Figure 5 shows another example for the trajectories related to the rotational levels of MgH ($v = 0$) at $N = 1$ and 24. Two aspects may be discerned. First, the MgH_2 collision complex for the high-N component is much more long-lived than that for the low-N component. Such behavior is unclear in the previous work because of the short time of termination for the trajectories. Second, for the high-N trajectory, the bending angle

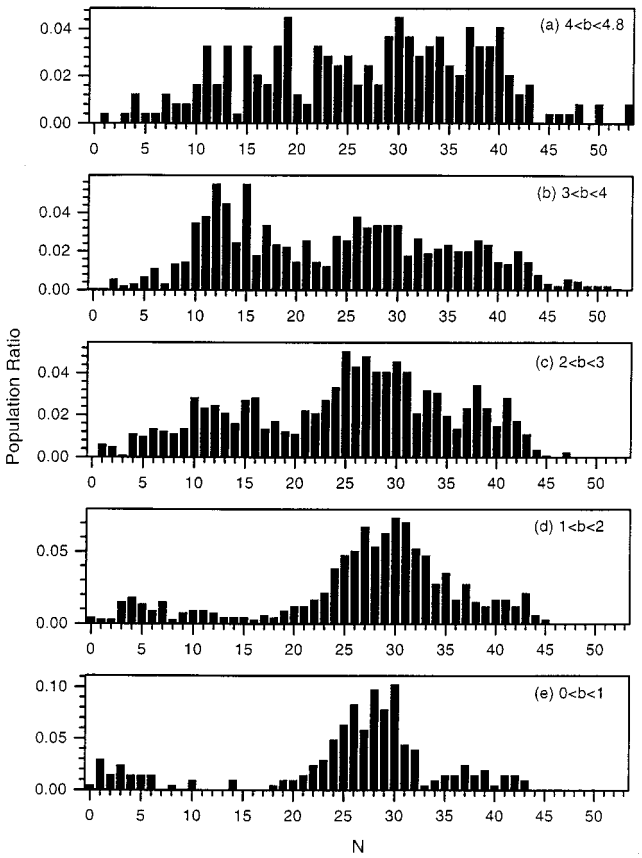

Figure 7. Rotational distributions of MgH ($v = 0$) vs b, the impact parameter. The initial kinetic energy is 2.026 kcal/mol, and H_2 is in $v = 0$ and $N = 1$. b lies in the regions (a) (4, 4.8) Å with 243 trajectories, (b) (3, 4) Å with 890 trajectories, (c) (2, 3) Å with 809 trajectories, (d) (1, 2) Å with 649 trajectories, and (e) (0, 1) Å with 204 trajectories.

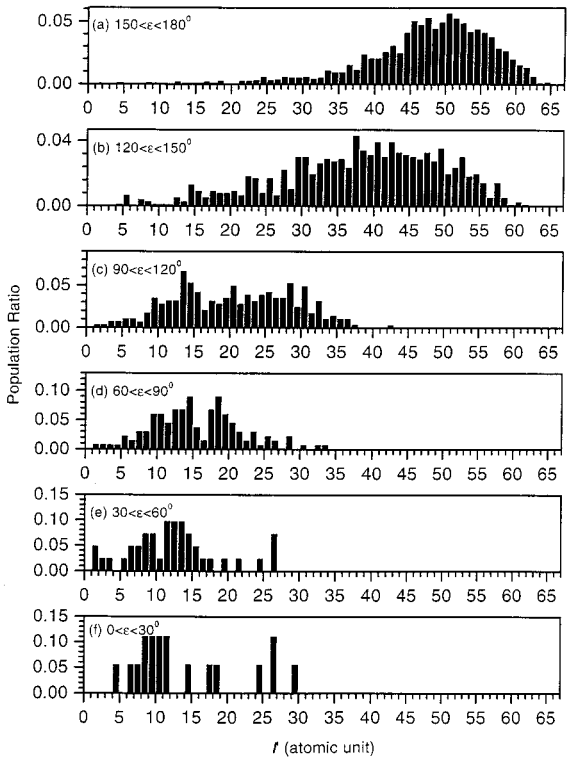

Figure 8. Orbital angular momentum $\mathbf{l}'$ of the MgH + H products vs ϵ, the relative angle between $\mathbf{l}'$ and $\mathbf{j}'$. The initial kinetic energy is 2.026 kcal/mol, and H_2 is in $v = 0$ and $N = 1$. ϵ lies in the regions (a) (150°, 180°) with 1555 trajectories, (b) (120°, 150°) with 764 trajectories, (c) (90°, 120°) with 284 trajectories, (d) (60°, 90°) with 133 trajectories, (e) (30°, 60°) with 41 trajectories, and (f) (0°, 30°) with 18 trajectories.

reaches 180° rapidly (Figure 5b,c), whereas for the low-N trajectory, the bending angle expands only to ca. 90° when the departing H atom is far from the MgH product (Figure 5a,c). The phenomenon confirms that the high-N component of the bimodal rotational distribution, affected by the strong anisotropy, is formed via a collinear complex before dissociating. In contrast, the low-N component is subject to a weaker anisotropic interaction; the departing H atom does so along the Mg−H stretching coordinate at a rate faster than that for the change of the HMgH angle.

B. Angular Momentum. The total angular momentum ($\mathbf{J}$) must be conserved during the reaction; i.e., $\mathbf{J} = \mathbf{j}' + \mathbf{l}'$, in which $\mathbf{j}'$ denotes the MgH angular momentum and $\mathbf{l}'$ the orbital angular momentum. According to our observation of 50 000 trajectories, the maximum $\mathbf{J}$ is 39.79 $\hbar$, and ca. 93% of the trajectories result in obtuse-angle (>90°) ϵ between $\mathbf{j}'$ and $\mathbf{l}'$ in the final products. Even so, the low-N and high-N components exhibit distinct vector correlation. In the following section, we examine the relation of the MgH distribution to the angle ϵ between $\mathbf{j}'$ and $\mathbf{l}'$, the impact parameter, b, and the orbital angular momentum, $\mathbf{l}'$. Figure 6 shows a plot of the rotational distributions versus the angles ϵ, which are divided into six groups with an interval of 30°. In general, if ϵ is acute (<90°), the MgH will be preferentially populated in the low-N levels, while both low-N and high-N levels can be populated if ϵ becomes obtuse. The high-N component dominates in the (150°, 180°) group. Figure 7 shows that the high-N component dominates at small b, especially when 0 Å $\leq b \leq$ 1 Å. With increasing b, the low-N component becomes enhanced, while the high-N population shows no sign of decay. As shown in Figure 8, $\mathbf{l}'$ appears to be small at an acute ϵ. Its average value is ca. 10−11 $\hbar$ when 0° $\leq \epsilon \leq$ 30°. $\mathbf{l}'$ then increases regularly with ϵ. The average $\mathbf{l}'$ increases to 50−51 $\hbar$ when ϵ lies in the (150°, 180°) region.

According to the information displayed in Figures 6−8, the formation of low-N and high-N components may be ascribed to the following vector correlation. First, at a small impact parameter (e.g., b < 1 Å), which leads to a small $\mathbf{J}$, a backward scattering (or rebound) is usually favored. The resulting $\mathbf{l}'$ turns out to be in the opposite direction to $\mathbf{J}$ (the initial $\mathbf{j}$ is considered to be small). Therefore, to conserve $\mathbf{J}$, the $\mathbf{j}'$ should be large enough to compensate for the $\mathbf{l}'$ contribution, and the obtained MgH tends to be populated in the high-N levels. This vector correlation is depicted in Figure 9a, in which the angle ϵ is obtuse. Note that $\mathbf{l}'$ has large magnitude when the angle ϵ is obtuse (Figure 8). Second, as b becomes large, $\mathbf{J}$ is large as well. Provided that the reactive scattering is forward, then $\mathbf{l}'$ has a similar direction as $\mathbf{J}$. If the obtained angle ϵ is acute, then $\mathbf{l}'$ has small magnitude (Figure 8), thereby leading to a small $\mathbf{j}'$ and the MgH population in the low-N levels. The interpretation is consistent with the result in Figure 6, showing that the probability for the high-N formation is little when ϵ is acute. The related vector correlation is depicted in Figure 9b. Third, at a large b, if the reactive scattering is forward and the obtained ϵ is obtuse, the magnitude of $\mathbf{l}'$ should be comparable to or even larger than $\mathbf{J}$ (Figure 8). To conserve $\mathbf{J}$, $\mathbf{j}'$ can vary largely depending on the angle, α, between $\mathbf{l}'$ and $\mathbf{J}$. The vector correlation for two extreme cases is depicted in Figure 9c,d. If α is small, $\mathbf{j}'$ turns out to be small, and the MgH population will be in the low-N levels. If α is large, $\mathbf{j}'$ should be large as well. The MgH will be in the high-N levels. Finally, it should be pointed out that we have oversimplified the complicated behavior of the reactive collision complex, treated it with a

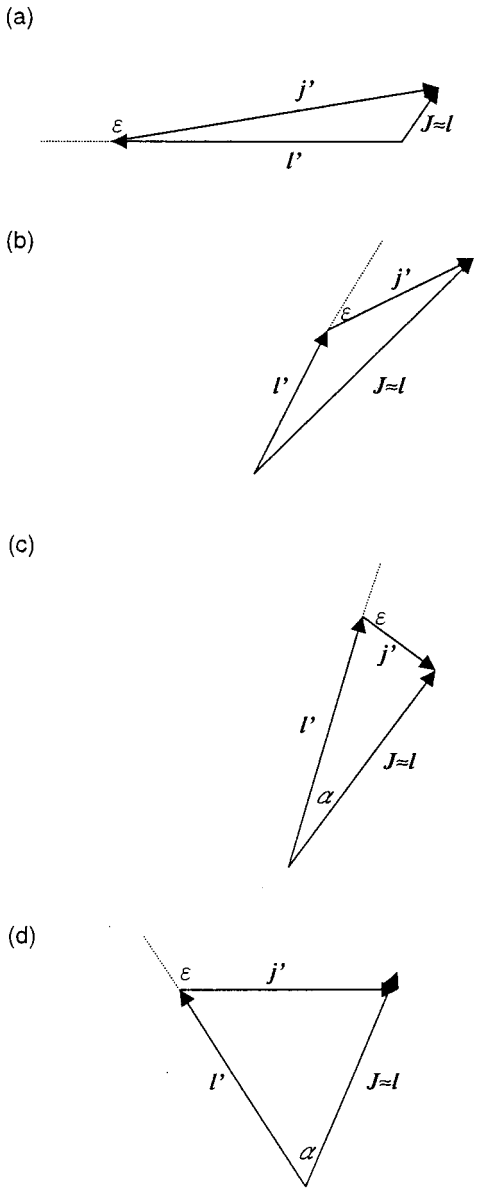

Figure 9. Vector correlation among **J**, **l′**, and **j′**. (a) and (d) denote the formation of the high-*N* levels and their corresponding vector correlation; (b) and (c) denote the formation of the low-*N* levels and their corresponding vector correlation.

model of elastic scattering, and discussed only the extreme cases. We believe that exceptions do exist.

IV. Conclusion

The QCT calculations for the $Mg(3^1P_1)$ with H_2 ($v = 0$, $N = 1$) reaction have been performed on more improved ab initio PESs in this work. We have constructed a new version of ab initio PESs for $2A'$and $1A'$ states and the corresponding fit energy functions. The current QCT calculations have resulted in more reliable dynamical parameters. The rotational bimodal distributions of MgH ($v = 0$ and 1) thus obtained are much more improved than those reported previously. The $1A'$ surface is characteristic of a small potential well in the region of $\theta \leq 40°$ and $r_3 \geq 3$ Å, which is not found in the old PES. This potential feature might enhance the population in the low-*N* levels. In this work, we have also provided information on the angular momentum analysis. The trajectory calculations show that the rotational distributions are closely related to the impact parameter and the relative angle between the orbital and the rotational angular momentum. The related vector correlation has been accordingly adopted to rationalize the formation of rotational bimodality.

Acknowledgment. This work is supported by the National Science Council of Taiwan, Republic of China under the Contract NSC89-2113-M-001-030.

References and Notes

(1) Blickensderfer, R. P.; Jordan K. D.; Adams, N.; Breckenridge, W. H. *J. Chem. Phys*. **1982**, *86*, 1930.

(2) Breckenridge W. H.; Umemoto H. *J. Chem. Phys*. **1984**, *80*, 4168.

(3) Kleiber, P. D.; Lyyra, A. M.; Sando, K. M.; Zafiropulos, S. V.; Stwalley, W. C. *J. Chem. Phys*. **1986**, *85*, 5493.

(4) Kleiber, P. D.; Lyyra, A. M.; Sando, K M.; Heneghan, S. P.; Stwalley, W. C. *Phys. Rev. Lett*. **1985**, *54*, 2003.

(5) Chaquin, P.; Sevin, A.; Yu, H. *J. Phys. Chem*. **1985**, *89*, 2813.

(6) Breckenridge, W. H.; Wang, J. H. *Chem. Phys. Lett*. **1987**, *137*, 195.

(7) Lin, K. C.; Huang, C. T. *J. Chem. Phys*. **1989**, *91*, 5387.

(8) Liu, D. K.; Chin, T. L.; Lin, K. C. *Phys. Rev. A* **1994**, *50*, 4891.

(9) Ou, Y. R.; Liu, D. K.; Lin, K. C. *J. Chem. Phys*. **1998**, *108*, 1475.

(10) Ou, Y. R.; Hung, Y. M.; Lin, K. C. *J. Phys. Chem. A* **1999**, *103*, 7938.

(11) Schinke, R. *Photodissociation Dynamics*; Cambridge University Press: Cambridge, 1993.

(12) Andresen, P.; Schinke, R. In *Molecular Photodissociation Dynamics*; Ashfold, M. N. R., Baggott, J. E., Eds.; Royal Society of Chemistry: London, 1987.

(13) Sorbie, K. S.; Murrell, J. N. *Mol. Phys*. **1975**, *29*, 1387.

(14) Murrell, J. N.; Carter, S.; Farantos, S. C.; Huxley, P.; Varandas, A. J. C. *Molecular Potential Energy Functions*; John Wiley & Sons: New York, 1984.

(15) Dunham, J. L. *Phys. Rev.* **1932**, *4*, 721.

(16) Chapman, S.; Bunker, D. L.; Gelb, A. *QCPE* **1974**, 273.

(17) Bunker, D. L. *Methods Comput. Phys.* **1971**, *10*, 287.

(18) Press, W. H.; Teukolsky, S. A.; Vetterling, W. T.; Flannery, B. P. *Numerical Recipes in Fortran 77*; Cambridge University Press: New York, 1992; Chapter 7.

(19) Smith, I. W. M. *Kinetics and Dynamics of Elementary Gas Reactions*; Butterworth: London, 1980; pp 89−94.

(20) Truhlar, D. G.; Muckerman, J. T. In *Atom-Molecule Collision Theory: A Guide for the Experimentalist*; Bernstein, R. B., Ed.; Plenum Press: New York, 1979.